THERMAL TRANSPORT IN THE DIII-D EDGE PEDESTAL

W. M. Stacey, (weston.stacey@nre.gatech.edu) Georgia Tech
Atlanta, GA 30332
&
R. J. Groebner, (groebner@fusion.gat.com), General Atomics Co.
San Diego, CA 92186
January, 2006

Abstract

A new procedure for inferring $\chi_{i,e}$ in the plasma edge from experimental data and integrated modeling code calculations has been developed which takes into account atomic physics and radiation effects and convective as well as conductive heat flux profiles. Application to DIII-D shots indicates that the sharp temperature gradient pedestal region may be caused as much, if not more, by an increase (with radius) of the conductive heat flux as by a decrease of the thermal transport coefficient. Inferred $\chi_{i,e}^{\exp}$ are compared with theoretical predictions.

PACS 52.55.Fi

I. Introduction

The physics of the steep-gradient, edge pedestal region in H-mode plasmas has been the subject of experimental investigation for many years (e.g. Refs. 1-8). The motivation for understanding the edge pedestal is based, at least in part, on calculations[9,10] which indicate that because of "stiffness" in temperature profiles the performance of future tokamaks will be sensitive to the value of the density and particularly the temperature at the top of the edge pedestal. Thus, understanding the edge pedestal characteristics is generally regarded to be a prerequisite for predicting the performance of future tokamaks.

Theoretical efforts to understand the edge pedestal have focused on several different aspects of the underlying physics. Investigations (e.g. Refs. 11-14) of the MHD stability of the edge pressure pedestal against ballooning and peeling (surface kink) modes have led to an understanding of edge pressure/pressure gradient limits leading to the onset of edge-localized-mode (ELM) instabilities which momentarily destroy the edge pedestal structure.

While the onset of MHD instabilities such as ELMs limit the maximum allowable value of the pressure or pressure gradient in the edge pedestal, they can not determine the structure of the pressure profile when the MHD instabilities are suppressed. Several other lines of investigation have been developed to the end of explaining (or at least modeling) the edge pedestal structure observed in the absence of or in between ELMs. The interaction of the plasma ion and neutral atom profiles has been shown to produce an edge pedestal structure in the former, under the assumption of diffusive particle transport[15]. The physical conservation (particle, momentum, energy), transport and atomic physics constraints have been shown to require a pedestal structure in the edge temperature and density profiles that agrees with experimental observation, when experimental rotation velocity and radial electric field profiles are used to evaluate the predicted pinch velocity[16,17]. A particle guiding center analysis[18] was employed to explain the pedestal formation in terms of the ionization of recycling neutrals, together with orbit squeezing and the presence of an X-point transport mechanism. Finally, particle and energy diffusion coefficients have simply been adjusted in transport

simulations of the plasma edge to obtain agreement with measured edge density and temperature profiles (e.g. Refs. 7, 8, 19 and 20). Other investigations have had the objective of combining MHD, transport and atomic physics mechanism to develop theory-based predictive algorithms for pedestal parameters such as width and height (e.g. Refs. 21 and 22).

The ion and electron thermal diffusivities are important parameters in any attempt to understand the edge temperature pedestals. Knowledge of these diffusivities to date comes almost entirely from their trial and error adjustment in transport simulations to obtain agreement with observed edge temperature profiles[7,8,16,17,19,20], although there have been some initial efforts to calculate edge thermal diffusivities from edge turbulence codes (e.g. Ref. 23). Such trial and error transport simulation fitting procedures are subjective, depend on the transport model and on the assumption about the split between convective and conductive heat fluxes, and do not provide much information about uncertainties in the inferred thermal diffusivities. Our purposes in this paper are 1) to present a more systematic procedure for inferring thermal diffusivities in the edge pedestal from experimental temperature profile data, 2) to apply this procedure to DIII-D H-mode shots with different edge parameters in order to infer ion and electron thermal diffusivity profiles in the edge pedestals and to elucidate the edge phenomena that affect these inferences.

II. Particle and Energy Transport in the Edge Pedestal

We have previously shown[16,17] that 1) the radial momentum balance requirement that the ion pressure gradient balances the forces due to the VxB and Er forces

$$\frac{\partial p_i}{\partial r} = n_i e_i \left(E_r + V_{\theta i} B_\phi - V_{\phi i} B_\theta \right) , \qquad (1)$$

and the use of the toroidal momentum balance leads to the requirement that the ion pressure gradient drive an outward ion flux that is sufficiently larger than the inward "pinch" ion flux (driven primarily by the radial electric field and rotation) that the net

outward ion flux satisfies the requirement of the continuity equation. This leads to a particle transport relation

$$L_{pi}^{-1} \equiv -\frac{1}{p_i}\frac{\partial p_i}{\partial r} = \frac{V_{ri} - V_{pinch}}{D_i} \tag{2}$$

where

$$V_{pinch,i} = \frac{\left[-M_{\phi i} - n_i e_i E_\phi^A + n_i m_i \left(\nu_{iI} + \nu_{di}^*\right)\left(f_p^{-1} V_{\theta i} + E_r \big/ B_\theta\right) - n_i m_i \nu_{iI} V_{\phi I}\right]}{n_i e_i B_\theta} \tag{3}$$

is of the form of a pinch velocity that can be evaluated using $M_{\phi i}$, the external momentum input (e.g. from neutral beams), E_ϕ^A, the induced toroidal electric field, ν_{iI}, the interspecies collision frequency, ν_{di}^* the total frequency for radial momentum transfer by viscous, inertial, atomic physics and 'anomalous' processes, $f_p \equiv B_\theta / B_\phi$, and the measured radial electric field and impurity toroidal rotation velocity. The only quantity that must be determined non-experimentally is the main ion poloidal rotation velocity, which can be estimated from the measured impurity poloidal rotation velocity or calculated. The quantity

$$D_i = \frac{m_i T_i \nu_{iI}}{\left(e_i B_\theta\right)^2}\left[1 + \frac{\nu_{di}}{\nu_{iI}} - \frac{Z_i}{Z_I}\right] \tag{4}$$

is of the form of a diffusion coefficient.

When measured rotation velocities and electric fields were used to evaluate Eq. (3) and thermal transport coefficients inferred from experiment were used to evaluate L_{Ti}, we have found[17] for several H-mode DIII-D shots that using Eq. (2) to integrate $-1/n_i\,(\partial n_i/\partial r) = L_{pi}^{-1} - L_{Ti}^{-1}$ yielded edge pedestal density profiles in good agreement with measured profiles. Thus, the next logical topics in this line of investigation would seem to be understanding the thermal and momentum transport and calculating rotation and the radial electric field in the edge plasma. This paper presents a more detailed investigation of thermal energy transport in the edge pedestal region of DIII-D H-mode plasmas. (Plans

for further investigation of momentum transport and the calculation of the electric field and rotation velocities in the edge plasma region are under development.)

The total ion and electron radial heat fluxes consist of conductive and convective components

$$Q_{i,e} = n_{i,e} T_{i,e} \chi_{i,e} L_{Ti,e}^{-1} + \frac{5}{2} \Gamma_{i,e} T_{i,e} \tag{5}$$

Thus, if $n_{i,e}, T_{i,e}$ and $L_{Ti,e}^{-1}$ are determined experimentally and $Q_{i,e}$ and $\Gamma_{i,e}$ are calculated from heat and particle balances, the experimental $\chi_{i,e}$ profile can be evaluated from

$$\chi_{i,e}(r) = L_{Ti,e}(r) \left[\frac{Q_{i,e}(r)}{n_{i,e}(r) T_{i,e}} - \frac{5}{2} \frac{\Gamma_{i,e}(r)}{n_{i,e}(r)} \right] \tag{6}$$

We note that this inference of $\chi_{i,e}$ depends not only on the measured temperature and density profiles and the total heat flux $Q_{i,e}$, but also on the convective heat flux.

We use an integrated modeling code system[24] that performs i) particle and power balances on the core plasma to determine the net particle and heat fluxes outward across the separatrix which are used as input to ii) an extended 2-point divertor model (with radiation and atomic physics) that calculates plasma densities and temperatures in the divertor and SOL and the ion flux incident on the divertor plate which iii) is recycled as neutral molecules and atoms that are transported (2D) through the divertor region across the separatrix into the plasma edge region. Any sources of gas puffed neutrals are also similarly transported inward. This integrated code system is used to calculate the ion particle and total heat fluxes crossing the sepatrix from the core into the SOL: Γ_{sep} = *beam particle source + recycling neutral particle source,* Q_{sep} *=beam + ohmic power input - core radiation.* We must at present estimate the split of Q_{sep} into Q_{sepi} and Q_{sepe}.

Using these values from the integrated model calculation as separatrix boundary conditions, we can then integrate the plasma ion particle balance equation

$$\frac{\partial \Gamma}{\partial r} = n_e n_o < \sigma \upsilon >_{ion} + S_{nb}, \qquad \Gamma(r_{sep}) = \Gamma_{sep}^{\exp} \tag{7}$$

where n_o is the density of recycling and gas fueling neutrals and S_{nb} is the source rate of plasma ions due to neutral beam (and pellet) injection, and the heat balance equations

$$\frac{\partial Q_i}{\partial r} = q_{nbi} - \frac{3}{2}(T_i - T_o^c) n_i n_o^c < \sigma\upsilon >_{cx+el} - q_{ie}, \qquad Q_i\left(r_{sep}\right) = Q_{sepi}^{\exp} \tag{8a}$$

and

$$\frac{dQ_e}{dr} = q_{nbe} + q_{ie} - n_e n_o < \sigma\upsilon >_{ion} E_{ion} - n_e n_z L_z, \qquad Q_e\left(r_{sep}\right) = Q_{sepe}^{\exp} \tag{8b}$$

inward from the separatrix to determine the edge distributions of $\Gamma(r)$ and $Q_{i,e}(r)$ needed to evaluate the radial distribution of $\chi_{i,e}$ from Eq. (6). Here $q_{nbi,e}$ is the local neutral beam power deposition density, n_o is the recycling neutral density, n_o^c is the density of 'cold' recycling neutrals that have not yet collided inside the separatrix and $1.5T_o^c$ is their average energy, $q_{ie} \sim \left(T_i - T_e\right)/T_e^{1.5}$ is the ion-electron equilibration rate, $E_{ion}(T_e, n_e)$ is the ionization energy, n_z is the impurity (carbon) density, $L_z\left(T_e, n_o\right)$ is the impurity radiation emissivity, $< \sigma\upsilon >_{cx+el}\left(T_i\right)$ is the charge-exchange plus elastic scattering rate coefficient, and $< \sigma\upsilon >_{ion}\left(T_e, n_e\right)$ is the electron impact ionization rate coefficient. The experimental $n_{e,z}$ and $T_{i,e}$ are used to evaluate the terms in Eqs. (7) and (8), which are then integrated radially inward from the experimental separatrix boundary conditions for the particle and heat fluxes determined as discussed above. The atomic physics data are taken from Ref. [25] and subsequent extensions to higher temperatures, and the radiation emissivity is calculated from a fit to coronal equilibrium calculations (taking into account the effect of charge-exchange and recombination in the presence of recycling neutrals) based on the ADPAC data[26].

III. Thermal Analysis of the Edge Pedestal in DIII-D Shots

A. Edge density and temperature profiles

Three shots with a range of edge parameters were chosen for detailed analysis. Shot 92976 (P_{nb} = 5.0 MW, δ = .33, q_{95} = 5.7, $n_{carb}/n_D = 1.5\%$) was a heavily gas puffed H-mode shot with a strong density pedestal and relatively low edge temperatures at 3212 ms just before MARFE'ing and making a H-L back transition immediately thereafter. Shot 97979 (P_{nb} = 6.5 MW, δ = .75, q_{95} = 3.9, $n_{carb}/n_D = 2.0\%$) was also a strongly gas puffed shot with high triangularity, sharp density and T_e pedestals and somewhat higher edge temperatures than shot 92976. It was in the middle of a robust H-mode phase at 3250 ms. Shot 118583 (P_{nb} = 9.2 MW, δ = .37, q_{95} = 3.8, $n_{carb}/n_D = 6.0\%$) was a lower density H-mode discharge with high pedestal temperatures, and was also gas fueled at the time considered. Pedestal density and temperatures and high order spline fits thereto are shown in Figs. 1-3. Spline fits were also constructed for gradient scale lengths L_{ne} and $L_{Ti,e}$.

To further characterize the plasma edge region, the parameters $\nu_{ei}^{*} \equiv \nu_{ei}\upsilon_{the}/qR$ and $\eta_{i,e} \equiv \frac{1}{T_{i,e}}\frac{\partial T_{i,e}}{\partial r}\Big/\frac{1}{n_{i,e}}\frac{\partial n_{i,e}}{\partial r}$ are shown in Fig. 4. The sharp decrease in $\eta_{i,e}$ in the pedestal region in shots 92976 and 97979 results from the much stronger density than temperature gradient. In shot 118583, $\eta_e \approx 2$ over the entire edge region, in agreement with the result reported for ASDEX-U[7], but this was not the case for the other two shots.

B. Edge cooling and heating profiles

The charge-exchange (plus elastic scattering) cooling rates of the plasma ions by cool incident neutrals from the plenum and scrape-off layer and the cooling rates of the plasma electrons by electron-impact ionization of incident neutrals and by radiation (line and recombination radiation of the carbon impurity and bremsstrahlung) are shown in Fig. 5 for the three shots. The edge peaking of the charge-exchange and ionization cooling are determined largely by the edge attenuation of uncollided (cool) and total neutral influxes, respectively. The edge peaking of the radiation cooling is due to a

combination of lower temperature and charge-exchange/recombination enhancement of the carbon radiation due to the high edge neutral concentration. The edge peaking of radiation cooling is larger for the low edge temperature shot 92976 than for the other two shots with higher pedestal electron temperatures. The radiation cooling is more important than the charge-exchange or ionization cooling except for the region just inside the separatrix in the low density shot 118583. The non-monotonic nature of q_{ie} is caused by the experimental $T_{i,e}$ profiles. There is no obvious correlation between the location of the pedestal in the electron temperature profile and either the radiation cooling or ionization cooling profiles, nor between the pedestal in the ion temperature profile and the peaking in the charge-exchange cooling profile.

C. Edge heat and particle flux profiles

These edge cooling phenomena significantly affect the edge profiles of $Q_{i,e}$ in the low-temperature/high-density shot 92976, but have relatively less effect in the other shots with higher edge temperatures and lower edge densities, as shown in Figs. 6. The ionization of incident neutrals has a large effect on the edge profile of Γ_i, as also shown in Figs. 6.

The magnitudes of $Q_{i,e}$ depend on net heat input to the core plasma and on the split between the electron and ion heat removal channels, which latter presently can not be determined experimentally. However, the particle fluxes $\Gamma_{i,e}$ can be determined from the integrated modeling code, as discussed above. For a given convective heat flux ($\frac{5}{2}\Gamma_{i,e}T_{i,e}$) profile, a range of physically allowable values of the ion-electron energy flux split, as characterized here by the parameter $(Q_e/(Q_e+Q_i))_{sep}$, can be determined from the requirement that the conductive heat fluxes must be everywhere non-negative. In our calculations, this condition requires that $(Q_e/(Q_e+Q_i))_{sep}$ be in the relatively narrow bands $0.50 \le (Q_e/Q)_{sep} \le 0.60$ for shot 92976 and $0.45 < (Q_e/Q)_{sep} < 0.55$ for shot 118583, but only within the relatively broad band $0.40 \le (Q_e/Q)_{sep} \le 0.80$ for shot

97979. The broader range of allowable values of $(Q_e/Q)_{sep}$ for shot 97979 than for the other two shots results from the significantly lower value of $\Gamma_{i,e}$ for this shot than for the other two.

The $Q_{i,e}$ profiles corresponding to limiting values of the allowable range of $(Q_e/Q)_{sep}$ are shown in Figs. 6 (except for shot 118583, for which only the value for $(Q_e/Q)_{sep} = 0.50$ is shown).

D. Edge convective heat flux fraction profiles

Corresponding to each value of the possible energy split within the allowable range of $(Q_e/(Q_e+Q_i))_{sep}$ there is a different split between the convective and conductive fractions of both the ion and electron heat fluxes. The convective fractions, $f_{conv}^{i,e} \equiv \left(2.5\Gamma_{i,e}T_{i,e}\right)/Q_{i,e}$, of the ion and electron energy fluxes are plotted in Figs. 7. The peaking of the convective energy fluxes and convective fractions just inside the separatrix is due to the ionization of incident neutrals.

For values of $(Q_e/(Q_e+Q_i))_{sep}$ larger than the upper limiting value [e.g. $(Q_e/(Q_e+Q_i))_{sep} >$ 60% for shot 92976] the total ion heat flux would become smaller than the convective ion heat flux and the ion convective fraction would become unphysical $\left(f_{conv}^{i} > 1\right)$ just inside the separatrix, as shown in Fig. 7a. For values of $(Q_e/(Q_e+Q_i))_{sep}$ smaller than the lower limiting value [e.g. $(Q_e/(Q_e+Q_i))_{sep} <$ 50% for shot 92976] the total electron heat flux would become smaller than the convective electron heat flux and the electron convective fraction would become unphysical $\left(f_{conv}^{e} > 1\right)$ in the flattop region, as also shown if Fig. 7a. Similar results are shown for shot 97979 in Fig. 7b.

It is clear from Figs. 7 that convective heat transport likely dominates conductive heat transport (convective fraction > 0.5) for ions and/or electrons over some portion of the plasma edge. This has profound implications for the inference of $\chi_{i,e}$, calling into

question inferences based on the common assumption that the heat flux is entirely conductive.

E. Edge heat diffusivity profiles

The profiles of $\chi_{i,e}$ inferred by using the experimental temperature and density profiles and the calculated heat and particle fluxes to evaluate Eq. (6) are shown in Figs. 8 and 9, for the limiting (92976, 97979) or median (118583) values of the allowable range of $Q_{esep}/(Q_i+Q_e)_{sep}$. The experimental values of $\chi_{i,e}$ must fall within the bounds formed by these limiting profiles. Also shown are the profiles of $\chi_{i,e}$ calculated from various approximate theoretical expressions (see appendix) using the experimental density and temperature data.

The experimentally inferred $\chi_i^{\exp}$ shown in Figs. 8 decreases in the steep-gradient pedestal region relative to the flattop region for shot 92976, consistent with the paradigm that the steep-gradient region is a "transport barrier" associated with a reduced $\chi_{i,e}$, but this is not the case for the other two shots. It is interesting that the inferred χ_i actually increases with radius in the inner part of the steep-gradient pedestal region for shots 97979 and 118583, and only decreases with radius in the very edge for shot 97979 and not at all for shot 118583. This happens because χ_i is proportional to the conductive heat flux, which in shot 97979 first increases with radius going into the steep-gradient region from the flattop region to compensate the decreasing convective ion heat flux fraction and only decreases just inside the separatrix to compensate the increasing convective heat flux due to ionization of recycling neutrals (Fig. 7b). In shot 118583, the monotonically increasing with radius conductive ion heat flux fraction (decreasing convective fraction in Fig. 7c) produces a monotonically increasing with radius inferred $\chi_i^{\exp}$ across the edge region (Fig.8c).

Somewhat different trends are seen in the inferred $\chi_e^{\exp}$ in Figs. 9. As shown in Figs. 7, the convective fractions of the electron heat flux generally decrease with radius across the entire edge region in all shots (except for a slight upturn just inside the

separatrix in shot 92976), requiring an increase in the conductive fractions, which would tend to cause $\chi_e^{\exp}$ inferred from Eq. (9) to increase with radius. The observation of slight dips in the $\chi_e^{\exp}$ profile in shots 92976 and 97979 is thus indicate of an electron "transport barrier", but the monotonic increase in $\chi_e^{\exp}$ with radius for shot 118583 (Fig. 9c) is not.

The same experimental temperature and density profiles were used to evaluate Eq. (6) when the assumption of radially uniform conductive heat flux was made. For all three shots, sharp dips in $\chi_{e,i}^{\exp}$ in the sharp-gradient pedestal region were calculated, as contrasted to the more accurate calculations taking into account also the profiles of the conductive and convective heat fluxes. Thus, the temperature pedestal (sharp gradient region) appears to be associated as much with a reduction in convective heat flux as with a reduction in $\chi_{i,e}$.

Profiles of theoretical $\chi_{e,i}^{th}$, based on using the experimental density and temperatures to evaluate the simple analytical formulas given in the appendix, are also given in Figs. 8 and 9. The neoclassical value, χ_i^{neo}, falls somewhat below the experimentally inferred range for χ_i throughout most of the edge region for shots 92976 and 118583, and somewhat above the experimentally inferred range for shot 97979, in reasonable agreement overall. Orbit squeezing corrections[27] (not included) would reduce χ_i^{neo} in the very edge. The $\eta_i - \mathrm{mod}\, e$ prediction is as much as an order of magnitude below the experimentally inferred range for shot 92976 and as much as an order of magnitude above for shot 118583 (except in the steep-gradient pedestal region), but is in reasonable agreement with experiment for shot 97979.

The trapped electron mode (TEM) χ_e^{TEM} generally overpredicts the experimentally inferred $\chi_e^{\exp}$ for the higher temperature shots 97979 and 118583, but is in reasonable agreement for the lower temperature shot 92976. The resistive ballooning mode predictions are generally "in the ballpark of" the inferred range for $\chi_e^{\exp}$.

These predictions of $\chi_{i,e}$ based on the simple theoretical expressions given in the appendix can only provide a rough indication of the level of transport associated with the

associated causative phenomenon. More sophisticated calculations are needed for a detailed comparison of theory and experiment, which is beyond the scope of this paper.

F. Discussion of uncertainties

The range of $\chi_{i,e}^{\exp}$ values determined above is sensitive to the ion-electron energy flux split (characterized here by the value of $(Q_e/(Q_e+Q_i))_{sep}$) and to the value of the convective heat flux. The ion-electron energy flux split in the edge depends on the energy transport and exchange in the core and can, in principle, be calculated if the energy transport and exchange mechanisms in the core are correctly modeled. We do not yet have available such a modeling capability that has been sufficiently checked against experiment, nor are we aware of such existing elsewhere. Also, as far as we know, no one has yet devised an experimental determination of the ion-electron energy flux split in the plasma edge. Further computational and experimental efforts to determine the ion-electron energy flux split in the plasma edge could provide the means to further narrow the range of experimentally inferred $\chi_{i,e}^{\exp}$.

Evaluation of the convective energy flux is rightfully regarded as difficult and uncertain, and we have taken pains with this aspect of the calculation. The particle flux in the edge was calculated by integrating the continuity equation inward from a separatrix ion particle flux boundary condition determined from a global particle balance on the plasma. The particle sources were from the neutral beams, which can be calculated accurately, and from the neutral influx resulting from gas fueling and recycling of plasma ions, which we calculated with a 2D neutral transport model, using ion fluxes from the plasma into the SOL to calculate incident ion fluxes on the divertor plate (with a "2-point" model including atomic physics and radiation) and using calculated charge-exchange neutral fluxes from the plasma edge, SOL and divertor to the wall to calculate neutral recycling from the chamber walls. The plasma flux into the SOL was calculated (iteratively) from the neutral beam and neutral influx fueling sources, using a "die-away" measurement[28] of particle confinement time in DIII-D. The fueling source was adjusted slightly to account for wall outgassing or absorption and modeling imperfections so that

the overall calculation predicted the measured line averaged density (i.e. the core fueling was correctly calculated). This neutral influx calculation has been found to be in reasonable agreement with measurements and Monte Carlo calculations in two DIII-D shots[29]. Nevertheless, experiments which provided for further validation of the neutral influx calculation would increase the confidence in the calculation of the convective heat flux and hence of the inference of $\chi_{i,e}^{\exp}$ in the plasma edge.

IV. SUMMARY AND CONCLUSIONS

An improved procedure for inferring $\chi_{i,e}^{\exp}$ in the plasma edge from measured temperature and density profiles and from the complementary results of an integrated modeling code has been developed and applied to three DIII-D H-mode shots. The procedure takes into account atomic physics and radiation effects on the edge particle and heat flux profiles, calculates both the convective and conductive electron and ion heat flux profiles, determines physically allowable values of the unknown split between the ion and electron heat fluxes in the edge, and evaluates therefrom a range of physically allowable $\chi_{i,e}^{\exp}$ profiles.

The sharp temperature gradient pedestal region in the edge of the 3 DIII-D shots examined was found to be caused as much, if not more, by an increase with radius of the conductive heat flux as by a decrease in heat transport coefficient.

Comparison of $\chi_{i,e}^{\exp}$ profiles with the predictions of simple analytical transport models showed that both neoclassical and η_i – mode theories for ion transport were in rough agreement with $\chi_i^{\exp}$, in magnitude if not profile, while the resistive balloning mode theory was generally in better agreement with measured $\chi_e^{\exp}$ than was the TEM theory for electron transport.

ACKNOWLEDGEMENT: This work was supported the U. S. Dept. of Energy Grant DE-FG02-00-ER54538 with the Georgia Tech Research Corporation and by U. S. Dept. of Energy Contract DE-AC03-99ER54463 with General Atomics Co. The authors are grateful to members of the DIII-D Team who took part in measuring and reducing the data used in this paper.

APPENDIX: THEORETICAL χ's

Neoclassical

The neoclassical expression for the ion thermal conductivity is[30]

$$\chi_i^{neo} = \varepsilon^{1/2} \rho_{i\theta}^2 \nu_{iz} \tag{A1}$$

In the presence of a strong shear in the radial electric field, the particle banana orbits are squeezed, resulting in a reduction in the ion thermal conductivity by a factor of $S^{-3/2}$, where[27]

$$S = \left| 1 - \rho_{i\theta} \left(\frac{d \ln E_r}{dr} \right) \left(\frac{E_r}{\upsilon_{thi} B_\theta} \right) \right| \tag{A2}$$

Here $\rho_{i\theta}$ is the ion poloidal gyroradius.

Ion temperature gradient modes

For a sufficiently large ion temperature gradient $\left(L_{Ti} < L_{Ti}^{crit} \simeq 0.1R \right)$ the toroidal ion temperature gradient (ITG) modes become unstable. An estimate of the ion thermal conductivity due to ITG modes is[31]

$$\chi_i^{itg} = \frac{5}{2} \left(\frac{1}{RL_{Ti}} \right)^{1/2} \left(\frac{T_e}{m_i} \right) \left(\frac{m_i}{e_i B} \right) \frac{1}{2} \rho_i \tag{A3}$$

where ρ_i is the gyroradius in the magnetic field B, and $k_\perp \rho_i = 2$ has been used..

Electron drift waves

The principal electron drift wave instabilities with $k_\perp c_s \leq \Omega_i$ arise from trapped particle effects when $\nu_e^* = \nu_e / (\nu_{the}/qR)\varepsilon^{3/2} < 1$. In more collisional plasmas the mode becomes a collisional drift wave destabilized by passing particles. An expression for the electron thermal conductivity that encompasses both the dissipative trapped electron mode (TEM) and the transition to the collisionless mode as $\nu_e^* \rightarrow 0$ is given by[30]

$$\chi_e = \frac{5}{2}\frac{\varepsilon^{3/2}}{\nu_e}\frac{c_S^2\rho_S^2}{L_n L_{Te}}\left(\frac{1}{1+0.1/\nu_e^*}\right) \tag{A4}$$

where c_s is the sound speed and $\rho_s = c_s/\Omega_i$, with Ω_i being the ion cyclotron frequency.

Resistive ballooning modes

Resistive ballooning modes can become unstable in the plasma edge, leading to a predicted thermal conductivity[32,33]

$$\chi_e^{RB} = \frac{R}{L_n}\left(q\rho_e\right)^2 \nu_{ei} \tag{A5}$$

REFERENCES

1. R. J. Groebner and T. H. Osborne, Phys. Plasmas, 5, 1800 (1998).
2. A. E. Hubbard, R. L. Boivin, R. S. Granetz, *et al.*, Phys. Plasmas, 5, 1744 (1998).
3. W. Suttrop, O. Gruber, B. Kurzan, *et al*., Plasma Phys. Control. Fusion, 42, A97 (2000).
4. T. H. Osborne, J. R. Ferron, R. J. Groebner, *et al*., Plasma Phys. Control Fusion, 42, A175 (2000).
5. A. E. Hubbard, Plasma Phys. Control. Fusion, 42, A283 (2000).
6. J. R. Ferron, M. S. Chu, G. L. Jackson, *et al.*, Phys. Plasmas, 7, 1976 (2000).
7. L. D. Horton, A. V. Chankin, Y. P. Chen, *et al*., Nucl. Fusion, 45, 856 (2005).
8. A. Kallenbach, Y. Andrew, M. Beurskens, *et al.,* Plasma Phys. Control. Fusion, 46, 431 (2004).
9. M. Kotschenreuther, W. Dorland, Q. P. Liu, *et al*., Proceedings of 16th Conf. Plasma Phys Control. Fusion Res., Montreal, 1996 (IAEA, Vienna, 1997), Vol. 2, p 371.
10. J. E. Kinsey, R. E. Waltz and D. P. Schissel, Proc. 24th Eur. Phys. Soc., Berchtesgarten, 1997, Vol. III, p 1081.
11. R. L. Miller, Y. R. Lin-Liu, T. H. Osborne and T. S. Taylor, Plasma Phys. Control. Fusion, 40, 753 (1998).
12. J. W. Connor, R. J. Hastie, H. R. Wilson and R. L. Miller, Phys. Plasmas, 5, 2687 (1998).
13. H. R. Wilson and R. L. Miller, Phys. Plasmas, 6, 873 (1999).
14. P. B. Snyder, H. R. Wilson, J. R. Ferron, *et al*., Phys. Plasmas, 9, 2037, (2002); also Nucl. Fusion, 44, 320 (2004).
15. R. J. Groebner, M. A. Mahdavi, A. W. Leonard, *et al*., Phys. Plasmas, 9, 2134 (2002); also Nucl. Fusion, 44, 204 (2004).
16. W. M. Stacey, Phys. Plasmas, 11, 1511 (2004); also 11, 4295 (2004); also 11, 5487 (2004).
17. W. M. Stacey and R. J. Groebner, Phys. Plasmas, 12, 042504 (2005); also to be published (2006).
18. C. S. Chang, S. Ku and H. Weitzner, Phys. Plasmas, 11, 2649 (2004).

19. G. D. Porter, R. Isler, J. Boedo and T. D. Rognlien, Phys. Plasmas, 7, 3663 (2000).
20. D. P. Coster, X. Bonnin, K. Borrass, *et al.*, *Proc. 18th Fusion Energy Conf., Sorrento, Italy, 2000* (IAEA, Vienna, 2001).
21. T. Onjun, G. Bateman, A. Kritz, *et al*., Phys. Plasmas, 9, 5018 (2002).
22. W. M. Stacey and R. J. Groebner, Phys. Plasmas, 10, 2412 (2003).
23. T. D. Rognlien, X. Q. Xu and R. H. Cohen, Plasma Phys. Control. Fusion, 42, A271 (2000).
24. W. M. Stacey, Phys. Plasmas, 5, 1015 (1998); also 8, 3673 (2001); also Nucl. Fusion, 40, 965 (2000).
25. W. M. Stacey, E. W. Thomas and T. E. Evans, Phys. Plasmas, 2, 3740 (1995); also 4, 678 (1997).
26. R. Hulse, Nucl. Technol./Fusion, 3, 259 (1983).
27. K. C. Shaing and R. D. Hazeltine, Phys. Fluids B, 4, 2547 (1992).
28. R. Maingi, M. A. Mahdavi, T. C. Jernigan, et al., Phys. Plasmas, 4, 1752 (1997).
29. W. M. Stacey, Nucl. Fusion, 40, 965 (2000).
30. J. A. Wesson, *Tokamaks,* 2nd ed. (Clarendon Press, Oxford, 1997).
31. F. Romanelli, W. M. Tang and R. B. White, Nucl. Fusion, 26, 1515 (1986).
32. P. N. Gudzar, J. F. Drake, D. McCarthy, et al., Phys. Fluids B, 5,3712 (1993).
33. D. Kalupin, M. Z. Tokar, B. Unterberg, et al., Nucl. Fusion, 45, 468 (2005).

FIGURE TITLES

1. Measured edge density and temperatures for shot 92976. (Solid line is spline fit.)
2. Measured edge density and temperatures for shot 97979. (Solid line is spline fit.)
3. Measured edge density and temperatures for shot 118583. (Solid line is spline fit.)
4. Collisionality parameter, η_i and η_e evaluated with measured density and temperatures.
5. Edge cooling and heating rates evaluated with measured density and temperatures.
6. Calculated edge heat and particle fluxes.
7. Calculated convective fractions of electron and ion edge heat fluxes.
8. Experimentally inferred ion heat diffusivity in plasma edge.
9. Experimentally inferred electron heat diffusivity in plasma edge.

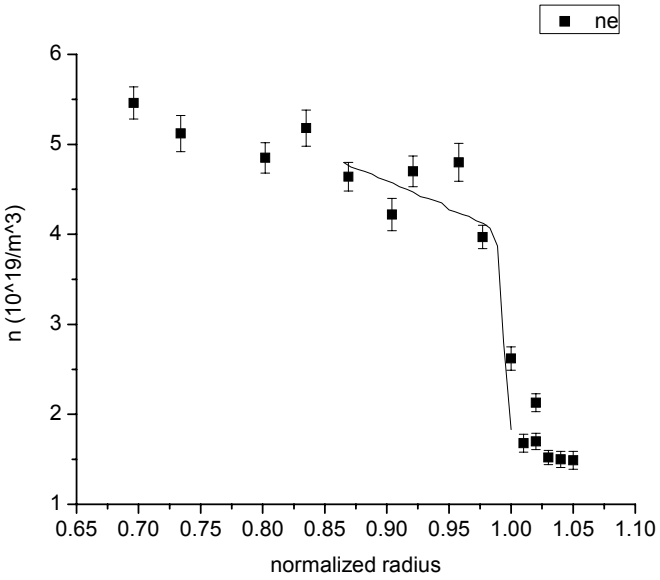
ne
n (10^19/m^3)
normalized radius
6
5
4
3
2
1
0.65
0.70
0.75
0.80
0.85
0.90
0.95
1.00
1.05
1.10

Fig. 1.a

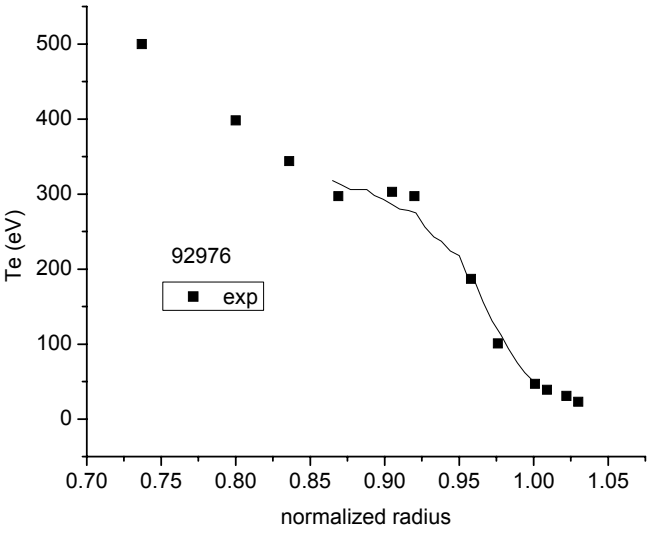
Te (eV)
normalized radius
92976
exp
500
400
300
200
100
0
0.70
0.75
0.80
0.85
0.90
0.95
1.00
1.05

Fig. 1.b

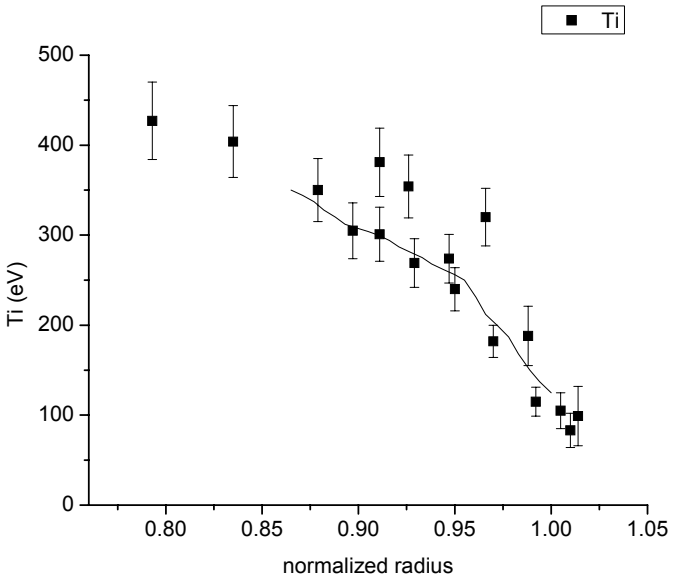
Ti
500
400
300
200
100
0
Ti (eV)
0.80
0.85
0.90
0.95
1.00
1.05
normalized radius

Fig. 1.c

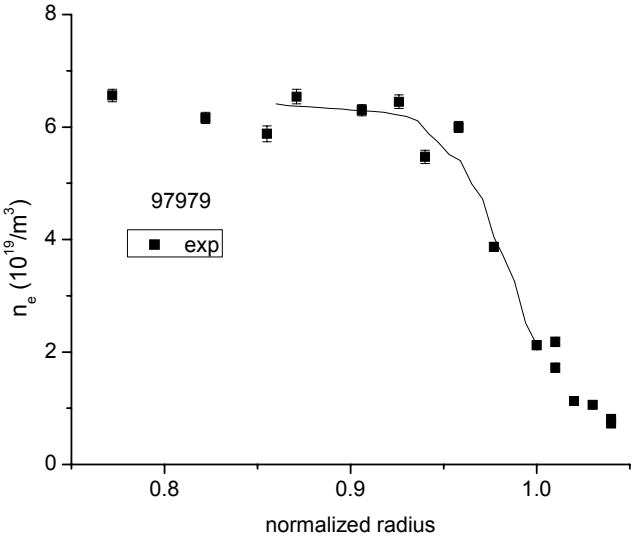
8
6
4
2
0
97979
exp
n_e (10^{19}/m^3)
0.8
0.9
1.0
normalized radius

Fig. 2a

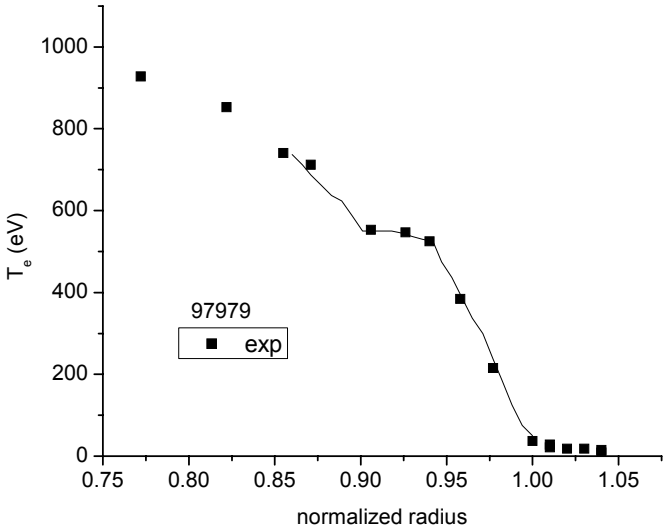
1000
800
600
400
200
0
T_e (eV)
97979
exp
0.75
0.80
0.85
0.90
0.95
1.00
1.05
normalized radius

Fig. 2b

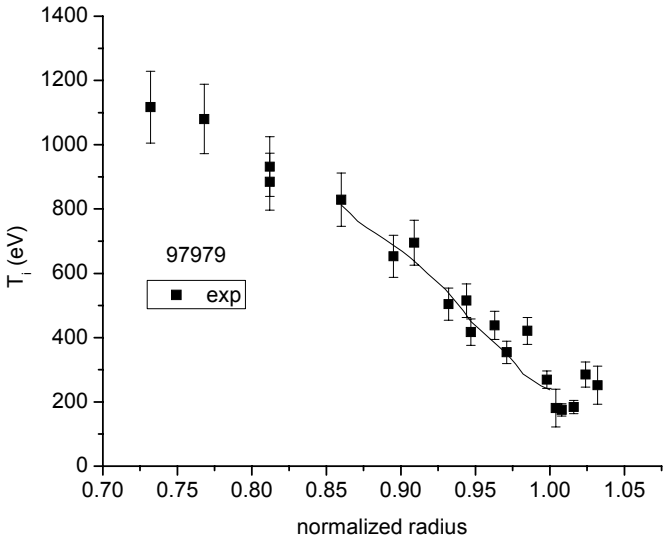
1400
1200
1000
800
600
400
200
0
T_i (eV)
97979
exp
0.70
0.75
0.80
0.85
0.90
0.95
1.00
1.05
normalized radius

Fig. 2c

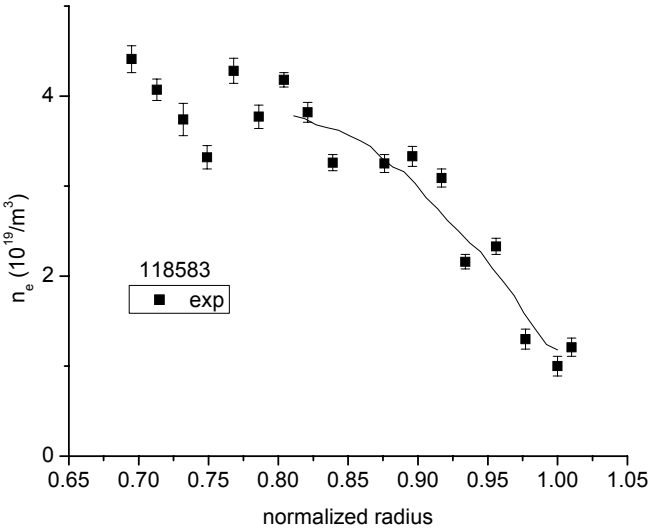
4
2
0
n_e (10^{19}/m^3)
118583
exp
0.65 0.70 0.75 0.80 0.85 0.90 0.95 1.00 1.05
normalized radius

Fig. 3a

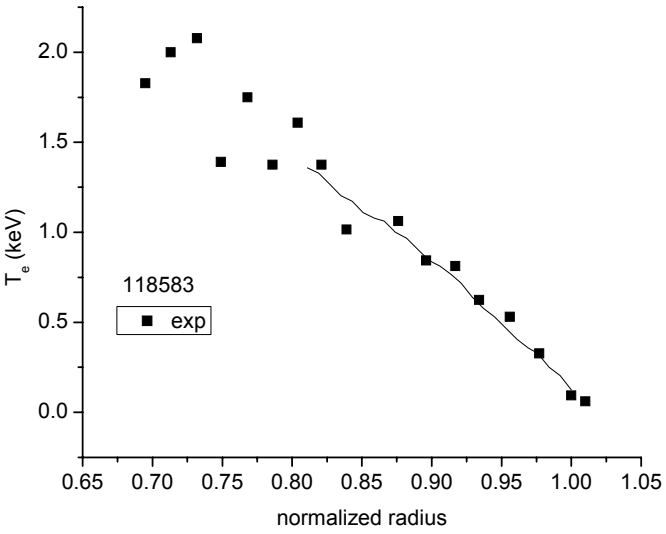
2.0
1.5
1.0
0.5
0.0
T_e (keV)
118583
exp
0.65 0.70 0.75 0.80 0.85 0.90 0.95 1.00 1.05
normalized radius

Fig. 3b

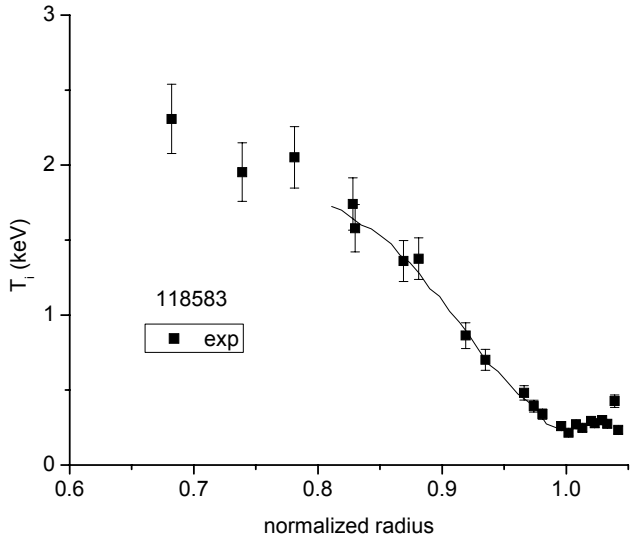
3
2
1
0
T_i (keV)
118583
exp
0.6
0.7
0.8
0.9
1.0
normalized radius

Fig. 3c

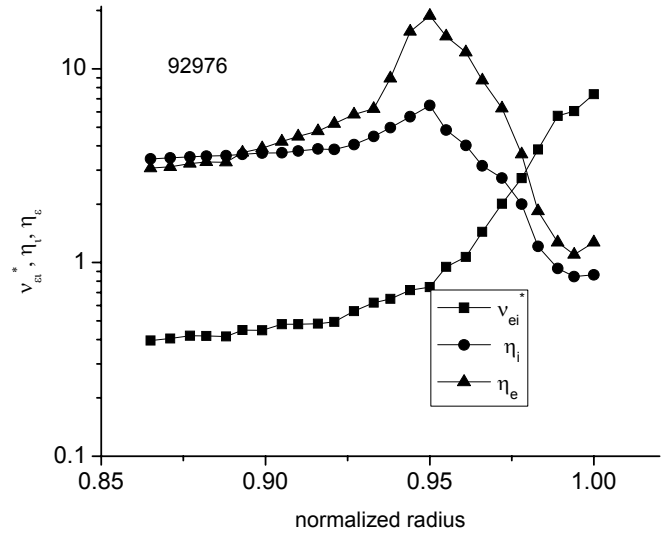
92976
10
1
0.1
ν^*_{ei}, η_i, η_e
ν^*_{ei}
η_i
η_e
0.85
0.90
0.95
1.00
normalized radius

Fig. 4a

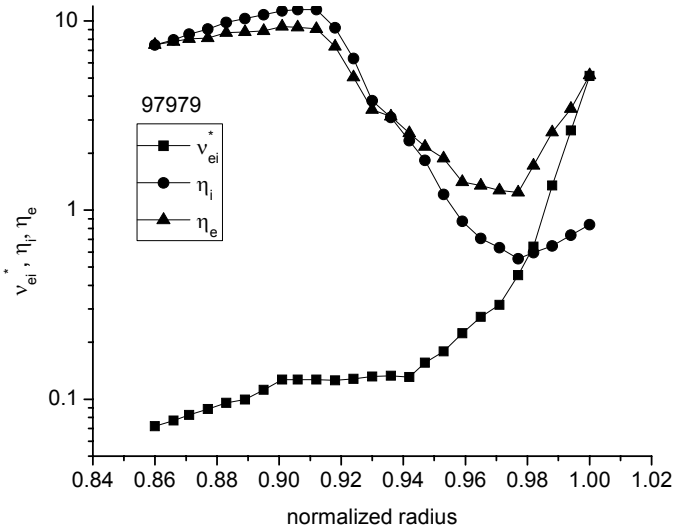
10
1
0.1
97979
ν^*_{ei}
η_i
η_e
ν^*_{ei}, η_i, η_e
0.84 0.86 0.88 0.90 0.92 0.94 0.96 0.98 1.00 1.02
normalized radius

Fig. 4b

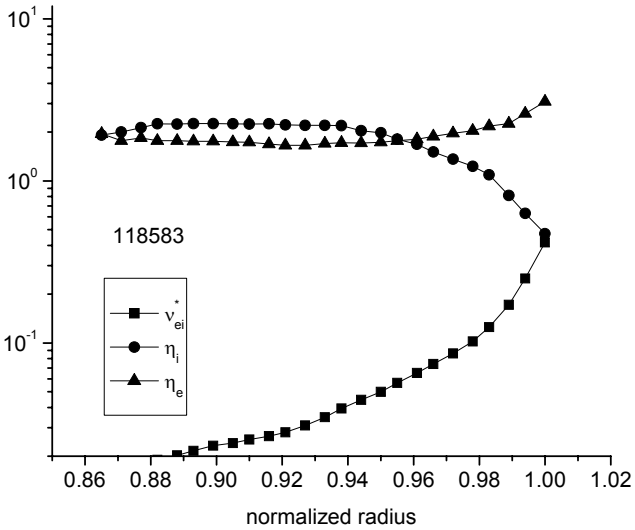
10^1
10^0
10^{-1}
118583
ν^*_{ei}
η_i
η_e
0.86 0.88 0.90 0.92 0.94 0.96 0.98 1.00 1.02
normalized radius

Fig. 4c

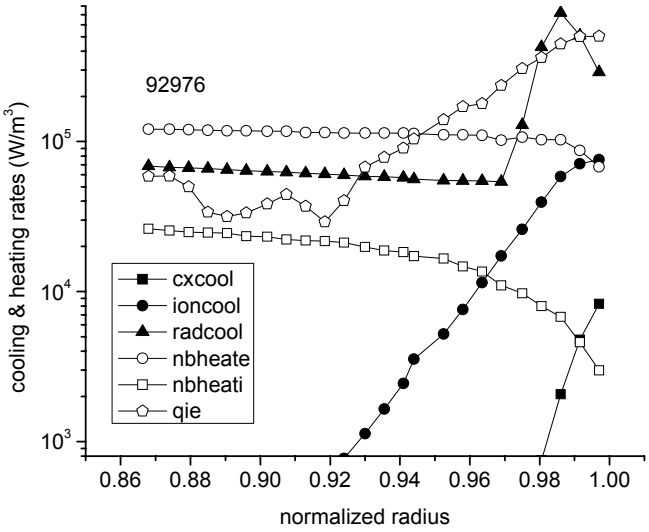
92976
cooling & heating rates (W/m^3)
10^5
10^4
10^3
cxcool
ioncool
radcool
nbheate
nbheati
qie
0.86
0.88
0.90
0.92
0.94
0.96
0.98
1.00
normalized radius

Fig. 5a

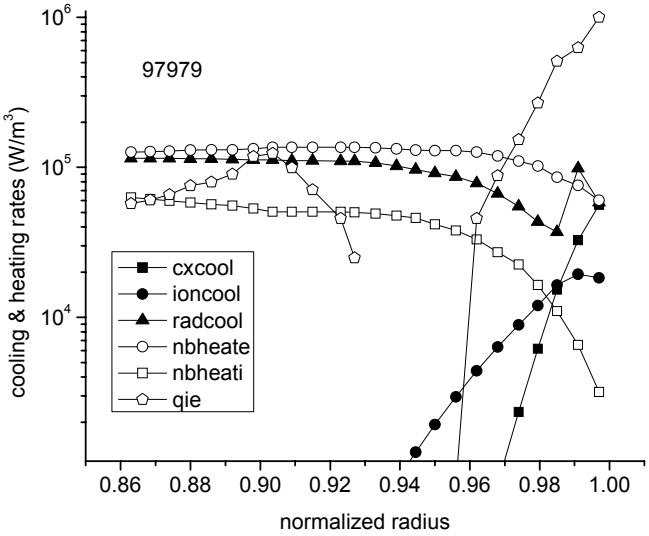
97979
cooling & heating rates (W/m^3)
10^6
10^5
10^4
cxcool
ioncool
radcool
nbheate
nbheati
qie
0.86
0.88
0.90
0.92
0.94
0.96
0.98
1.00
normalized radius

Fig. 5b

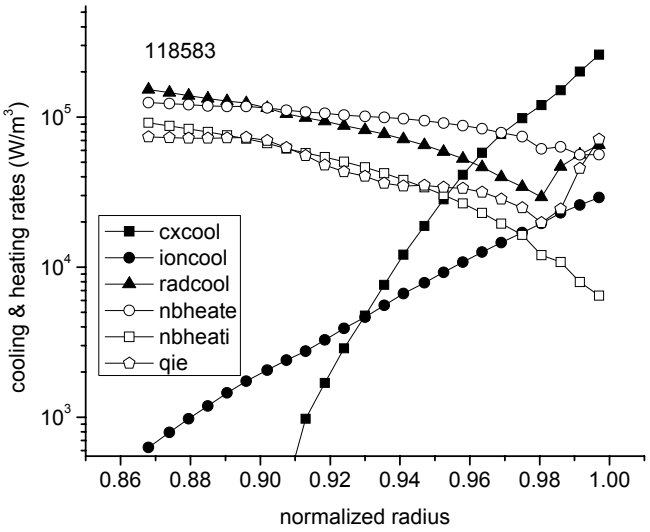
118583
cooling & heating rates (W/m^3)
10^5
10^4
10^3
cxcool
ioncool
radcool
nbheate
nbheati
qie
0.86
0.88
0.90
0.92
0.94
0.96
0.98
1.00
normalized radius

Fig. 5c

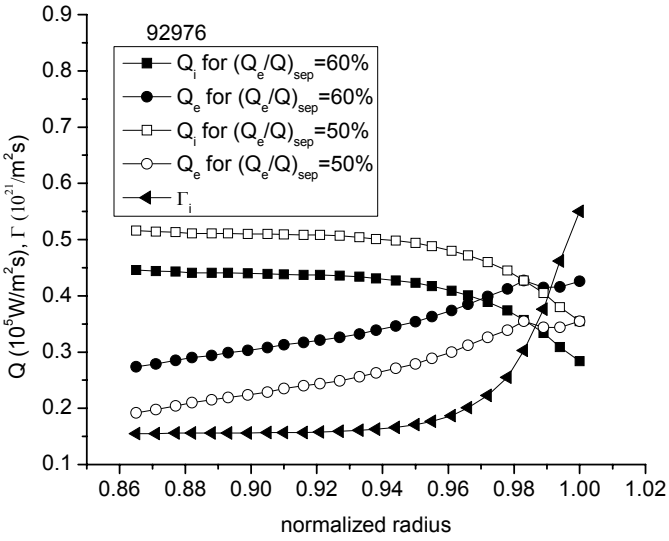
92976
Q_i for $(Q_e/Q)_{sep}$=60%
Q_e for $(Q_e/Q)_{sep}$=60%
Q_i for $(Q_e/Q)_{sep}$=50%
Q_e for $(Q_e/Q)_{sep}$=50%
Γ_i
Q (10^5W/m^{2}s), Γ (10^{21}/m^{2}s)
0.9
0.8
0.7
0.6
0.5
0.4
0.3
0.2
0.1
0.86
0.88
0.90
0.92
0.94
0.96
0.98
1.00
1.02
normalized radius

Fig. 6a

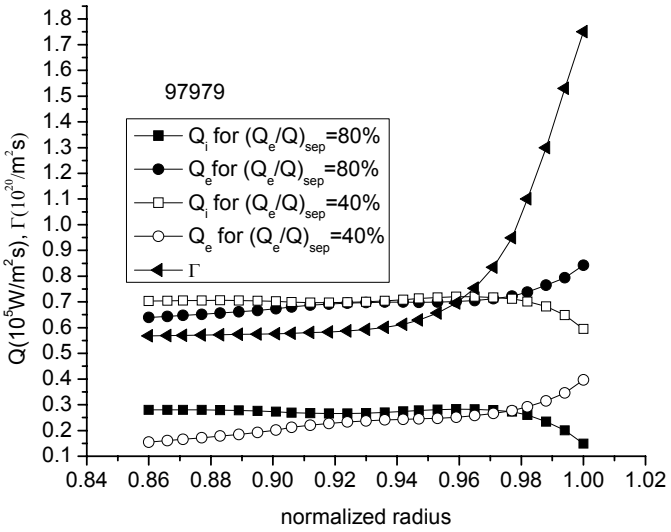
97979
Q_i for (Q_e/Q)_sep=80%
Q_e for (Q_e/Q)_sep=80%
Q_i for (Q_e/Q)_sep=40%
Q_e for (Q_e/Q)_sep=40%
Γ
Q(10^5W/m^2s), Γ(10^20/m^2s)
normalized radius

Fig. 6b

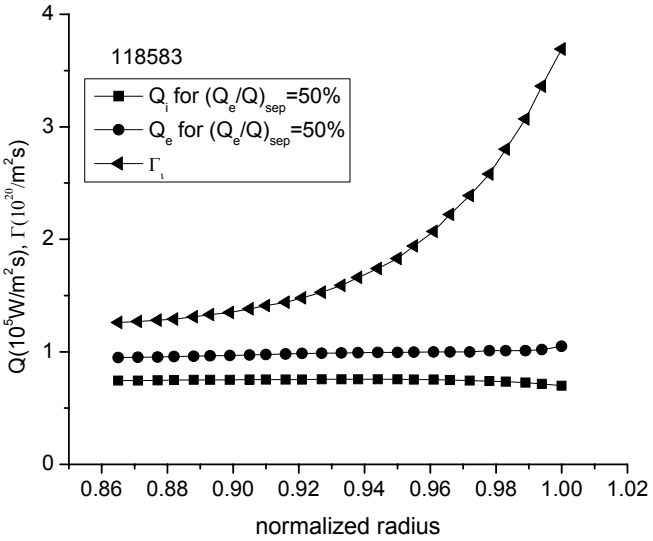
118583
Q_i for (Q_e/Q)_sep=50%
Q_e for (Q_e/Q)_sep=50%
Γ_t
Q(10^5W/m^2s), Γ(10^20/m^2s)
normalized radius

Fig. 6c

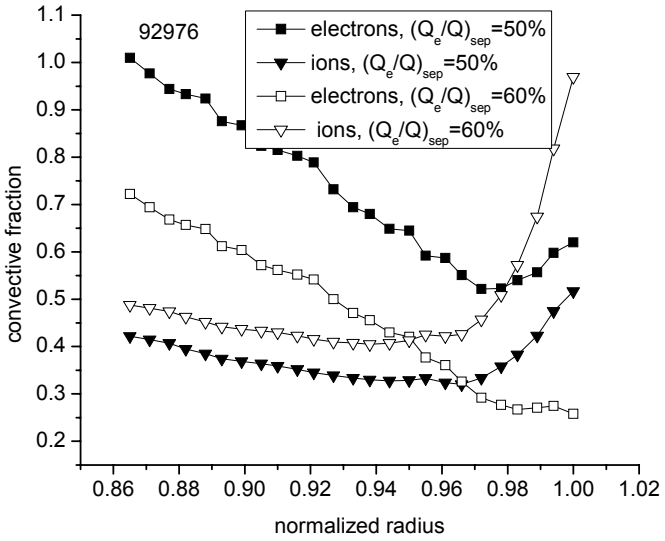
92976
electrons, (Qe/Q)sep=50%
ions, (Qe/Q)sep=50%
electrons, (Qe/Q)sep=60%
ions, (Qe/Q)sep=60%
convective fraction
normalized radius

Fig. 7a

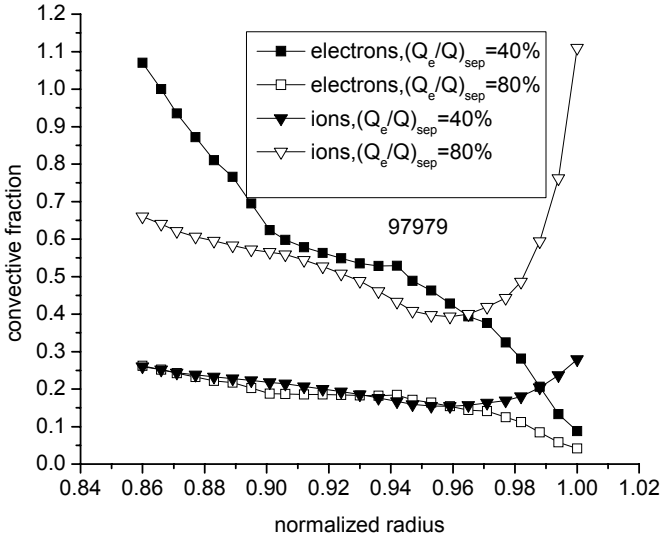
electrons,(Qe/Q)sep=40%
electrons,(Qe/Q)sep=80%
ions,(Qe/Q)sep=40%
ions,(Qe/Q)sep=80%
97979
convective fraction
normalized radius

Fig. 7b

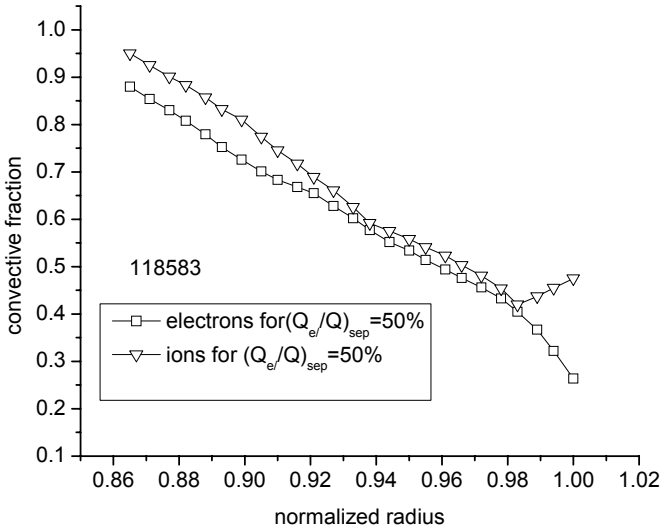
convective fraction
normalized radius
118583
electrons for(Qe/Q)sep=50%
ions for (Qe/Q)sep=50%

Fig. 7c

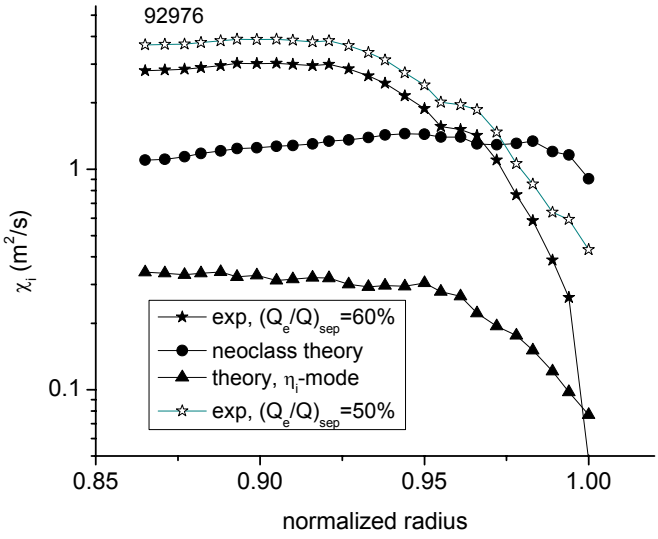
92976
χi (m2/s)
normalized radius
exp, (Qe/Q)sep=60%
neoclass theory
theory, ηi-mode
exp, (Qe/Q)sep=50%

Fig. 8a

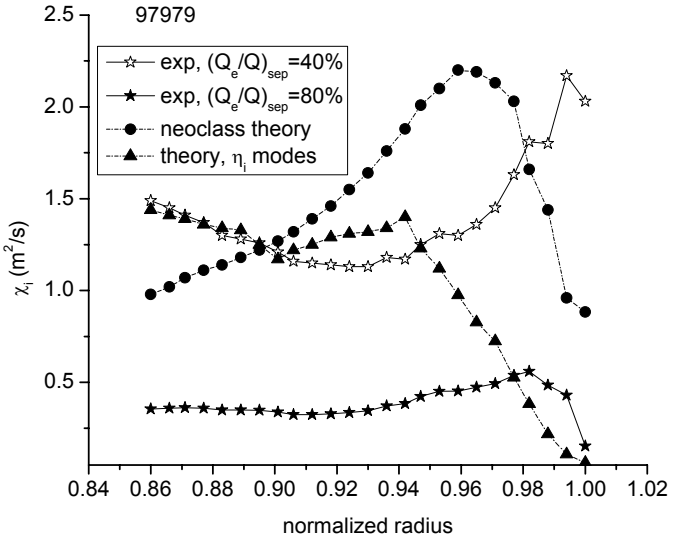
97979
exp, (Qe/Q)sep=40%
exp, (Qe/Q)sep=80%
neoclass theory
theory, ηi modes
χi (m2/s)
normalized radius

Fig. 8b

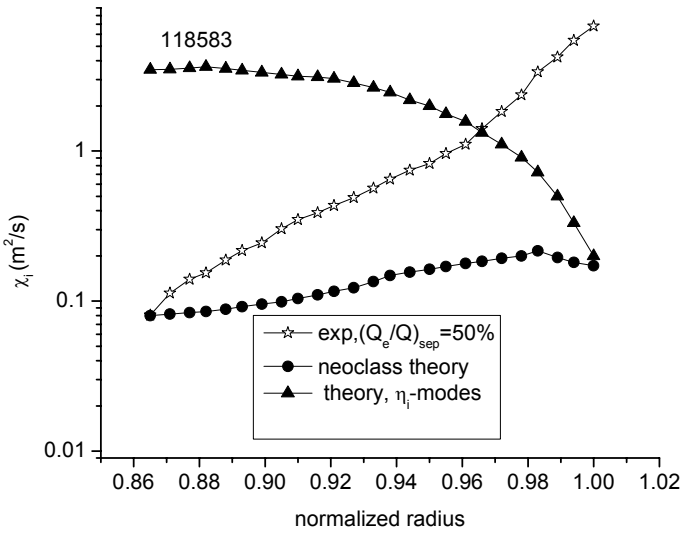
118583
exp,(Qe/Q)sep=50%
neoclass theory
theory, ηi-modes
χi (m2/s)
normalized radius

Fig. 8c

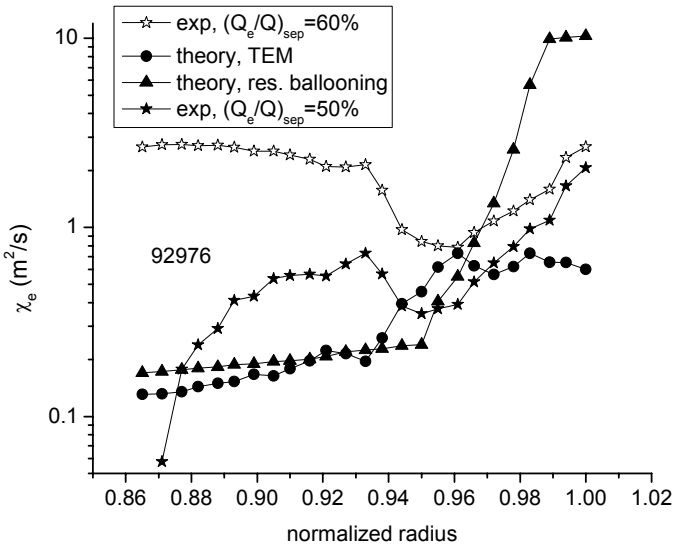
exp, (Qe/Q)sep=60%
theory, TEM
theory, res. ballooning
exp, (Qe/Q)sep=50%
92976
χe (m2/s)
normalized radius

Fig. 9a

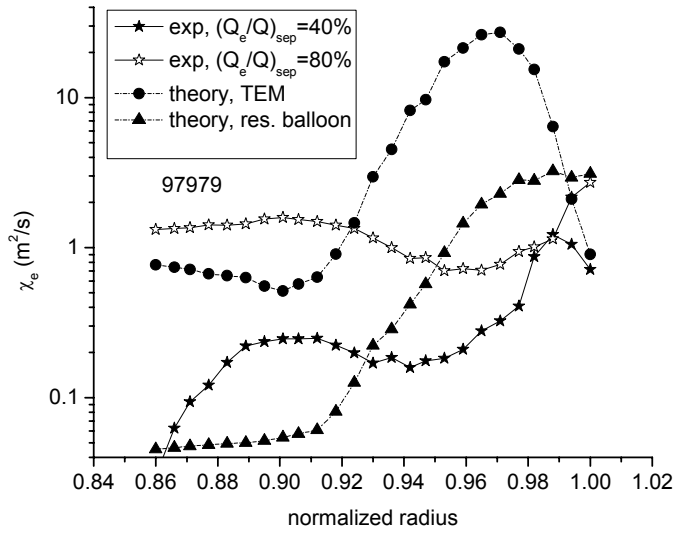
exp, (Qe/Q)sep=40%
exp, (Qe/Q)sep=80%
theory, TEM
theory, res. balloon
97979
χe (m2/s)
normalized radius

Fig. 9b

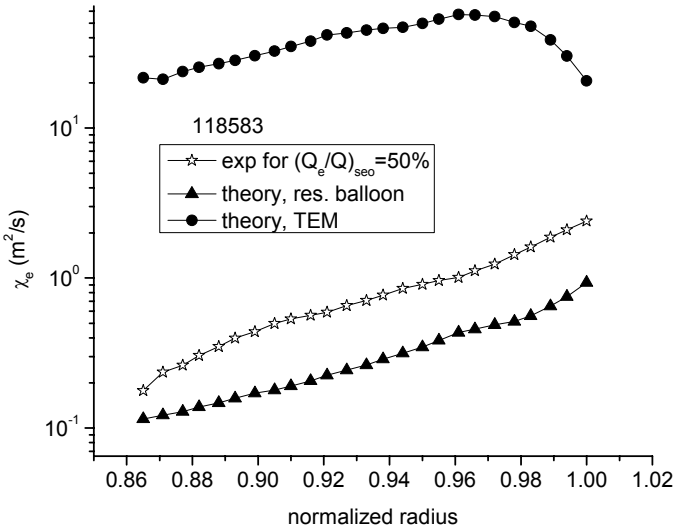
118583
exp for (Qe/Q)seo=50%
theory, res. balloon
theory, TEM
χe (m2/s)
10^1
10^0
10^-1
0.86
0.88
0.90
0.92
0.94
0.96
0.98
1.00
1.02
normalized radius

Fig. 9c